RSC Advances

PAPER

View Article Online
View Journal | View Issue

Cite this: *RSC Adv.*, 2024, **14**, 20867

Effect of a mesoporous $NiCo_2O_4$ urchin-like structure catalyzed with a surface oxidized $LiBH_4$ system for reversible hydrogen storage applications†

Ajaijawahar Kaliyaperumal, Gokuladeepan Periyasamy, Iyakutti Kombiah and Karthigeyan Annamalai *

A mesoporous $NiCo_2O_4$ urchin-like structure was synthesized by applying a facile hydrothermal method. Different concentrations of $NiCo_2O_4$ urchin-like structures were mixed with a surface oxidized $LiBH_4$ system using a wet-impregnation method, followed by heat treatment. The hydrogen storage capacity of $LiBH_4$ + 25% $NiCo_2O_4$, $LiBH_4$ + 50% $NiCo_2O_4$ and $LiBH_4$ + 75% $NiCo_2O_4$ systems was investigated. Typically, hydrogenated $LiBH_4$ + 25% $NiCo_2O_4$, $LiBH_4$ + 50% $NiCo_2O_4$ and $LiBH_4$ + 75% $NiCo_2O_4$ systems desorbed 2.85 wt%, 3.78 wt% and 3.91 wt% of hydrogen, respectively, at the dehydrogenation temperature ranging from room temperature (RT) to 275 °C. Further, the $LiBH_4$ + 75% $NiCo_2O_4$ system exhibited better kinetics than other systems and released ~5.8 wt% of hydrogen at a isothermal dehydrogenation temperature of 250 °C in 60 minutes. Hydrogen binding energies were calculated as 0.28 eV, 0.27 eV and 0.26 eV for $LiBH_4$ + 25% $NiCo_2O_4$, $LiBH_4$ + 50% $NiCo_2O_4$ and $LiBH_4$ + 75% $NiCo_2O_4$ systems, respectively. Moreover, the calculated activation energies of $LiBH_4$ + 25% $NiCo_2O_4$, $LiBH_4$ + 50% $NiCo_2O_4$ and $LiBH_4$ + 75% $NiCo_2O_4$ systems are 17.99 kJ mol^{-1}, 17.03 kJ mol^{-1} and 16.92 kJ mol^{-1}, respectively. The calculated BET (Brunauer–Emmett–Teller) surface area of $NiCo_2O_4$ and $LiBH_4$ + 75% $NiCo_2O_4$ systems is 124.05 and 136.62 m^2 g^{-1}, respectively. These results showed that hydrogen sorption and desorption properties are significantly increased by the influence of mesoporous structure, lower binding energy and activation energy of $LiBH_4$ + 75% $NiCo_2O_4$ system.

Received 5th March 2024
Accepted 18th June 2024

DOI: 10.1039/d4ra01709a

rsc.li/rsc-advances

1 Introduction

In the current scenario, over 80% of the global energy supply is obtained from conventional non-renewable fossil fuels, including natural gas, coal and petroleum sources.[1,2] The use of fossil fuels releases greenhouse gases and other polluting substances that seriously harm the environment.[3] Hydrogen has been recognized as a abundant, clean, economical and efficient energy source for a wide range of applications, including stationary supplies, distribution and various transportable hydrogen-fuelled systems. Hydrogen is an excellent long-term option to overcome the energy-based environmental issues, due to its advantages of high energy density (120 MJ kg^{-1}). During the energy conversion process, it just produces water as an output product.[4–7] However, the primary challenge among them is the absence of suitable techniques for storing the hydrogen. Moreover, storing hydrogen using traditional methods, such as compression and liquefaction, requires tremendous pressure and/or very low temperatures, which in turn increases the chances of leakage and safety issues.[8,9]

Solid-state hydrogen storage is a feasible technique to achieve future hydrogen storage goals considering its safety conditions, compactness and efficiency compared to conventional hydrogen storage systems.[10,11] Hydrogen can be bound either physically or chemically with different storage materials, which has a definite advantages in the aspects of safety and efficiency.[12,13] In recent decades, $LiBH_4$ has been widely explored[14,15] as a reversible hydrogen storage material for on-board energy carrier applications owing to its high volumetric and gravimetric hydrogen densities. Its slow kinetics, higher dehydrogenation temperature and severe reversible conditions (600 °C/35 MPa H_2) are major concerns. This behaviour can be associated with its high thermal stability and poor catalytic activity.[16] The complex hydrides $LiBH_4$,[17–21] $NaBH_4$,[22,23] and LiH[24] are extremely sensitive to air/moisture in the ambient atmosphere. These materials react instantly with water through exothermic reactions. Therefore, the certain operating conditions such as dry air and inert atmosphere are required to

Hydrogen Storage Materials and Nanosensors Laboratory, Department of Physics and Nanotechnology, College of Engineering and Technology, SRM Institute of Science and Technology, Kattankulathur, Chengalpattu, Tamil Nadu, India, 603203. E-mail: karthiga@srmist.edu.in; Tel: +91 9841615368

† Electronic supplementary information (ESI) available. See DOI: https://doi.org/10.1039/d4ra01709a

prevent the dehydrogenation of raw materials. Consequently, it is essential to understand how raw materials behave under moisture conditions. To manage the reactivity and unfavourable impacts at each stage of the industrial process, including storage, manufacturing, handling and processing, many possible reaction strategies are suggested for handling $LiBH_4$ under ambient atmospheric conditions according to the report by Goudon *et al.*[17] However, for on-board applications, the reversibility of $LiBH_4$ is still challenging.[25,26]

Recently, transition metal oxides have been used to improve the reversible hydrogen storage performance of complex hydrides through nanoconfinement and nanocatalytic effects. Some experimental studies involving $LiBH_4$ with transition metal oxides have been reported for hydrogen storage applications.[27–29] Zhang and his co-workers[30] reported that the re-hydrogenated (at 400 °C under 4.5 MPa) $LiBH_4$/M-Fe_2O_3/TiF_3 system absorbed ~4.27 wt% of hydrogen within 60 minutes. In a previous study, ~1.7 wt% hydrogen uptake capacity for $LiBH_4$–$2LiNH_2$-0.05/$3Co_3O_4$ systems was found under rehydrogenation conditions of 25–220 °C and 110 bar H_2 pressure.[31] Additionally, the dehydrogenated $LiBH_4$/SiO_2/TiF_3 system reabsorbed ~1.2 wt% of hydrogen at 300 °C within 233 minutes under 4.5 MPa.[32] Au *et al.*[33] investigated the reversibility of $LiBH_4$/TiO_2 and $LiBH_4$/V_2O_3 systems at 600 °C under 100 bar H_2 pressure with the hydrogen uptake capacities of 7.8 wt% and 7.9 wt%, respectively. Zang and his colleagues[34] reported the destabilization of the $LiBH_4$ system by $NiCo_2O_4$ nanorods. The mesoporous $NiCo_2O_4$ nanorods were mixed with $LiBH_4$ in different mass ratios (2 : 1, 1 : 1, 1 : 2) using the ball milling technique in a controlled atmosphere. As shown in their report, they directly dehydrogenated the raw $LiBH_4$ system using the $NiCo_2O_4$ structure and did not hydrogenate and rehydrogenate the $LiBH_4$–$NiCo_2O_4$ composites. Additionally, the *in situ* Co (Ni) and Co–B (Ni–B) are formed as intermediates during dehydrogenation. In this study, we used the surface oxidized $LiBH_4$ system and mixed it with mesoporous $NiCo_2O_4$ urchin-like structure in different weight percentages ($LiBH_4$ + 25% $NiCo_2O_4$, $LiBH_4$ + 50% $NiCo_2O_4$ and $LiBH_4$ + 75% $NiCo_2O_4$) by applying a simple wet-impregnation technique under lab atmospheric conditions. Moreover, we studied hydrogenation and dehydrogenation experiments systematically. From the hydrogenation and dehydrogenation results, it was found that no new phases were introduced into the $LiBH_4$/$NiCo_2O_4$ systems. Cabo *et al.* and Zhang *et al.* found that Ni and Co are good candidates for hydrogen storage due to their variable valence and higher Pauling's electronegativity than Mn, Fe, Ti and other metals. It is reasonable to infer that $NiCo_2O_4$, Co_3O_4 and NiO have a notable influence on improving the hydrogen sorption/desorption properties of the MgH_2 and $LiBH_4$ systems. The aforementioned reports mostly present the destabilization effect of the $LiBH_4$ system with sufficient hydrogen release at high temperatures.[28,31,35] However, they have not been performed effectively in the reversible hydrogen storage process. Furthermore, nanostructured metal oxides present numerous advantages due to the hierarchical arrangement of pore structures with sizes ranging from nanometres to micrometres and catalytic activity. Moreover, the favourable hydrogen release mechanism depends on the mesoporous materials with large surface areas owing to more active sites to assist the dissociation/recombination of H_2 molecules.[36,37] Butt *et al.*

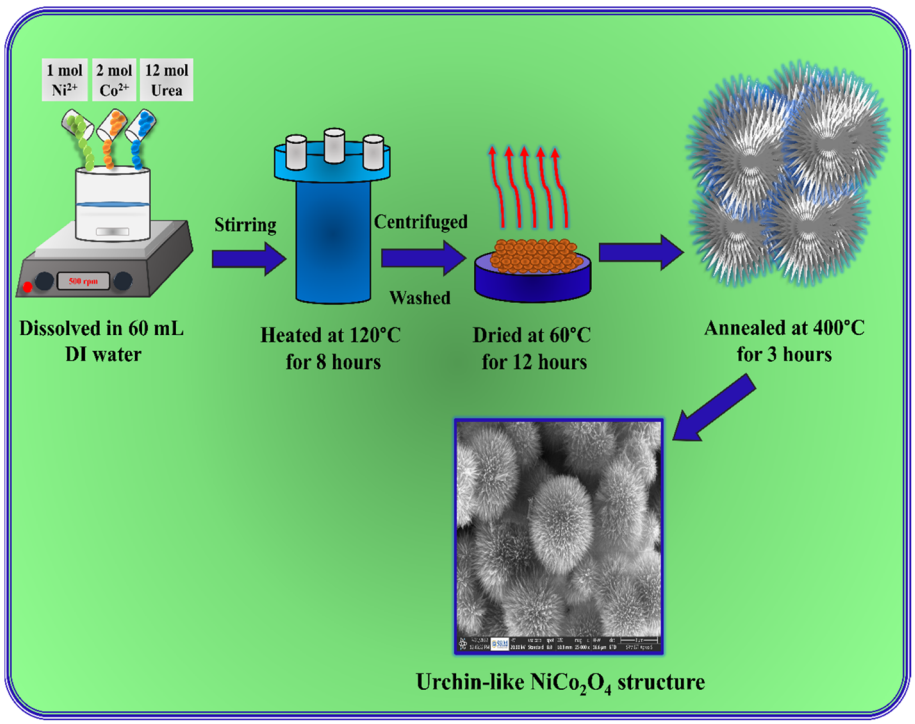

Fig. 1 Schematic representation of the preparation of an urchin-like $NiCo_2O_4$ structure.

investigated the hydrogen storage properties of hierarchical ZnV_2O_4 (ref. 38) and $Zn_2V_2O_7$ (ref. 39) nanostructures, which absorbed 1.76 and 1.21 wt% of H_2 under 5 MPa at 200 °C, respectively.

Under these scenarios, the present study focuses on investigating the hydrogen sorption/desorption performance of a mesoporous urchin-like $NiCo_2O_4$ structure catalyzed using a surface oxidized (air-sensitized) $LiBH_4$ system. From our previously reported study of the hydrogen storage properties of a surface oxidized $LiBH_4$ system catalyzed with NiO nanoflower,[19] we adopted nanorods and nanoplates.[40] Herein, the $NiCo_2O_4$ structure was prepared using the hydrothermal method, and $LiBH_4/NiCo_2O_4$ systems were prepared using the ultrasonic-assisted wet-impregnation method. From scanning electron microscopy (SEM) and transmission electron microscopy (TEM) assessments, the mesoporous $NiCo_2O_4$ structure was found to have an urchin-like formation. According to Kang *et al.*,[41] the surface oxidized $LiBH_4$ could reduce the dehydrogenation and activation energy barrier during hydrogen desorption. In addition, the surface oxidation effects help to reach thermodynamically predicted temperatures for dehydrogenation reactions.[40,42,43] In this study, it is observed that mesoporous $NiCo_2O_4$ with a surface oxidized $LiBH_4$ system presents an outstanding storage performance. Notably, 5.8 wt% of hydrogen was desorbed using a $LiBH_4$ + 75% $NiCo_2O_4$ system in isothermal dehydrogenation at 250 °C for 60 minutes. Moreover, the weak chemical binding nature and activation energy of the $LiBH_4/NiCo_2O_4$ systems are discussed based on thermogravimetric analysis. Additionally, possible reaction mechanisms are discussed.

2 Experimental section

2.1 Materials

The commercial chemical $LiBH_4$ was purchased from Sigma-Aldrich with ≥95.0% purity. Additional chemicals $Ni(NO_3)_2 \cdot 6H_2O$, $Co(NO_3)_2 \cdot 6H_2O$, $CO(NH_2)_2$, diethyl-ether (DEE) and ethanol were purchased from Siscon Research Laboratory, India, and used without further purification.

2.2 Methods

2.2.1 Synthesis of nickel cobalt oxide. In a typical hydrothermal process, 1 mol $Ni(NO_3)_2 \cdot 6H_2O$ and 2 mol $Co(NO_3)_2 \cdot 6H_2O$ were dissolved in 60 mL distilled water, and 12 mol urea was added into the solution under continuous stirring for 60 minutes. Then, the solution was transferred into a 100 mL Teflon-lined stainless-steel autoclave and heated at 120 °C for 8 hours. After cooling to room temperature, the precipitate was centrifuged and washed several times with water and ethanol. Then, the precipitate was dried at 60 °C for 12 hours. Finally, the $NiCo_2O_4$ was obtained after annealing at 400 °C for 3 hours in air. Fig. 1 shows a schematic representation image of the urchin-like $NiCo_2O_4$ structure preparation.

2.2.2 Synthesis of $LiBH_4/NiCo_2O_4$ systems. $LiBH_4/NiCo_2O_4$ systems were prepared using the wet-chemical impregnation method under ambient atmospheric conditions. Surface oxidized $LiBH_4$ + 25% $NiCo_2O_4$ was dispersed in 30 mL of diethyl ether (DEE). The mixed solution was sonicated in a bath sonicator for 2 hours. Then, the resultant mixture was dried at 100 °C using a hotplate with vigorous stirring for solvent evaporation. The $LiBH_4$ + 50% $NiCo_2O_4$ and $LiBH_4$ + 75% $NiCo_2O_4$ were also prepared by applying the aforementioned procedure. Later, $LiBH_4$ + 25% $NiCo_2O_4$, $LiBH_4$ + 50% $NiCo_2O_4$ and $LiBH_4$ + 75% $NiCo_2O_4$ mixtures were annealed at 275 °C for 1 hour under argon atmosphere.

2.3 Hydrogen sorption and desorption experiments

Before hydrogenation, the thermal stability of $LiBH_4/NiCo_2O_4$ systems was confirmed by applying the TG-STA under an argon atmosphere. Then, 10–20 mg of the sample was placed in the

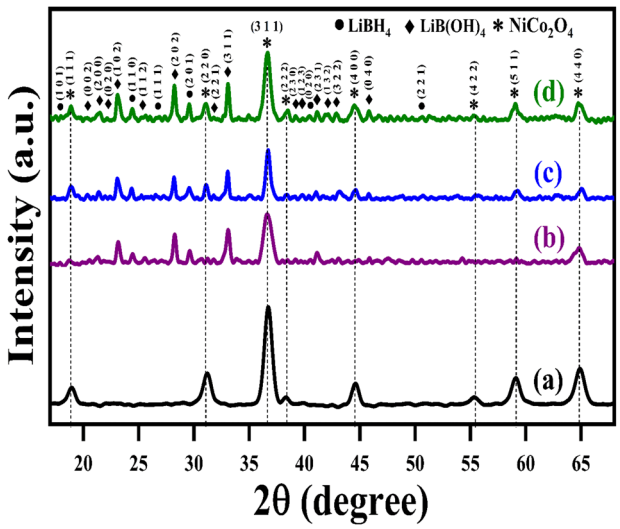

Fig. 2 XRD patterns of (a) $NiCo_2O_4$, (b) $LiBH_4$ + 25% $NiCo_2O_4$, (c) $LiBH_4$ + 50% $NiCo_2O_4$, and (d) $LiBH_4$ + 75% $NiCo_2O_4$ systems.

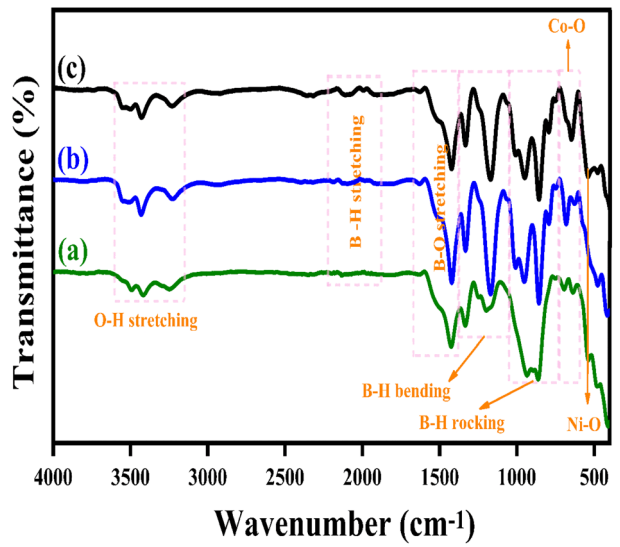

Fig. 3 FTIR patterns of (a) $LiBH_4$ + 75% $NiCo_2O_4$, (b) $LiBH_4$ + 50% $NiCo_2O_4$,and (c) $LiBH_4$ + 25% $NiCo_2O_4$ systems.

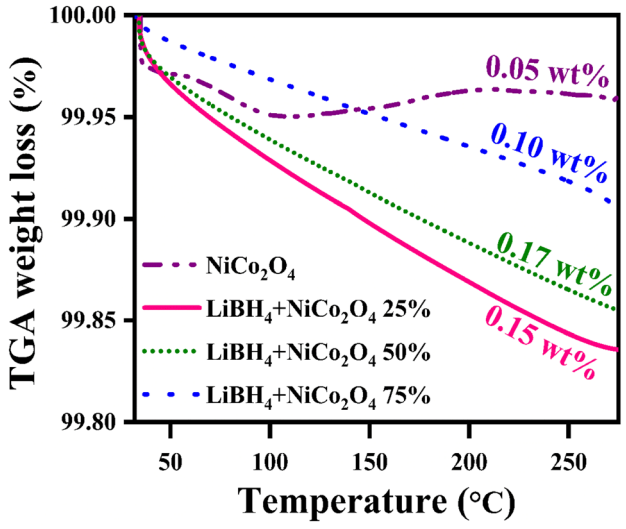

Fig. 4 Thermal stability curves of $NiCo_2O_4$, $LiBH_4$ + 25% $NiCo_2O_4$, $LiBH_4$ + 50% $NiCo_2O_4$ and $LiBH_4$ + 75% $NiCo_2O_4$ systems before hydrogenation.

hydrogenation chamber of the custom-built hydrogenation setup. Next, the sample was hydrogenated at 150 °C for 30 minutes under 4, 6 and 10 bar H_2 pressure conditions. Immediately, the hydrogenated sample was transferred to the TG-STA for dehydrogenation from RT to 275 °C with a 15 °C min^{-1} rate under an argon gas flow of 100 mL min^{-1}. Additionally, isothermal dehydrogenation experiments were performed at 250 °C for 1 hour using argon medium with 100 mL min^{-1} flow for the hydrogenated samples (at 150 °C for 30 minutes under 10 bar H_2 pressure).

3 Results and discussion

3.1 Structural and functional group analyses

The structural analysis of $NiCo_2O_4$ and $LiBH_4/NiCo_2O_4$ samples was performed using the powder X-ray diffraction (PXRD) technique. As shown in Fig. 2a, the diffracted peaks of $NiCo_2O_4$ indexed at 18.7°, 31.2°, 36.6°, 38.3°, 44.5°, 55.3°, 59.3° and 65.2°, corresponding to the (1 1 1), (2 2 0), (3 1 1), (2 2 2), (4 0 0), (4 2 2), (5 1 1) and (4 4 0) planes, respectively, are matched with standard data of JCPDS card no. #20-0781. The calculated average crystallite size is ~26 nm. Further, the lattice constant values are found to be $a = b = c = 8.11$ Å for the $NiCo_2O_4$ structure. Fig. 2b–d shows that the XRD spectra of $LiBH_4$ + 25% $NiCo_2O_4$, $LiBH_4$ + 50% $NiCo_2O_4$ and $LiBH_4$ + 75% $NiCo_2O_4$ systems indicate the presence of $LiBH_4$ (JCPDS card no. #27-0287), $LiB[OH]_4$ (JCPDS card no. 01-075-1156) and $NiCo_2O_4$

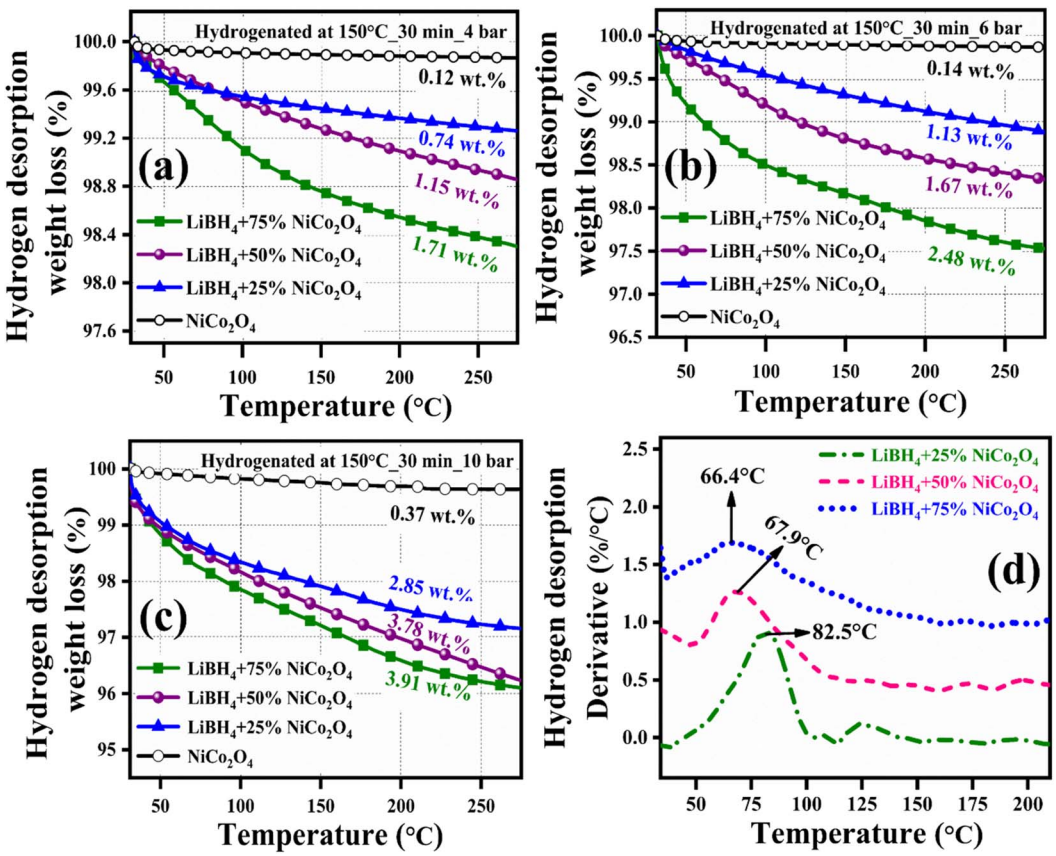

Fig. 5 Non-isothermal hydrogen desorption curves of $NiCo_2O_4$, $LiBH_4$ + 25% $NiCo_2O_4$, $LiBH_4$ + 50% $NiCo_2O_4$ and $LiBH_4$ + 75% $NiCo_2O_4$ systems: (a) Hydrogenated at 150 °C for 30 min under 4 bar, (b) hydrogenated at 150 °C for 30 min under 6 bar, and (c) hydrogenated at 150 °C for 30 min under 10 bar; (d) H_2 desorption derivative TG curves of hydrogenated (150 °C for 30 min under 10 bar) $LiBH_4$ + 25% $NiCo_2O_4$, $LiBH_4$ + 50% $NiCo_2O_4$ and $LiBH_4$ + 75% $NiCo_2O_4$ systems.

(JCPDS card no. #20-0781) phases. According to the results, it is clear that increasing the concentration of $NiCo_2O_4$ in the system produced an increased peak intensity. Additionally, the combined phases of borohydroxide ($B[OH]_4^-$) and borohydride (BH_4^-) were identified in the systems due to the surface oxidation of $LiBH_4$.

Fig. 3(a–c) illustrates the Fourier Transform Infrared Spectroscopy (FTIR) patterns of $LiBH_4$ + 75% $NiCo_2O_4$, $LiBH_4$ + 50% $NiCo_2O_4$, and $LiBH_4$ + 25% $NiCo_2O_4$ systems. The characteristic bands of Ni–O and Co–O are observed at 551 and 645 cm^{-1},[44] respectively, originating from the stretching vibration modes of the spinel $NiCo_2O_4$ structure. In addition, the vibration modes, such as O–H stretching (3592–3180 cm^{-1}),[19] B–H stretching (2484–2196 cm^{-1}),[45] B–O stretching (1559–1375 cm^{-1}),[19] B–H bending (1367–1007 cm^{-1})[45] and B–H rocking (867–681 cm^{-1}),[19] can be observed in the spectra, confirming the presence of $NiCo_2O_4$, $LiBH_4$ and $LiB[OH]_4$. The air exposure of $LiBH_4$ caused the existence of $B[OH]_4$.

3.2 Hydrogen desorption analysis

Before hydrogenation, the thermal stability of the systems was investigated using a thermal analyzer. As shown in Fig. 4, negligible 0.05, 0.17, 0.15 and 0.10 wt% of weight losses were observed in the systems, from RT to 275 °C. After confirming the thermal stability, all hydrogen sorption measurements were carried out at 150 °C for 30 minutes under 4 bar H_2 pressure. The hydrogenated systems were dehydrogenated using a thermal analyzer from RT to 275 °C under an argon medium at a heating rate of 15 °C min^{-1}. During non-isothermal hydrogen desorption, the hydrogenated $NiCo_2O_4$ system released 0.12 wt% of hydrogen, while the $LiBH_4$ + 25% $NiCo_2O_4$, $LiBH_4$ + 50% $NiCo_2O_4$ and $LiBH_4$ + 75% $NiCo_2O_4$ systems gradually released 0.74, 1.15 and 1.71 wt% hydrogen, respectively, from RT to 275 °C in argon atmosphere (Fig. 5a). The hydrogen storage behaviour of the systems was analysed by increasing the hydrogenation conditions of 6 and 10 bar H_2 pressures separately under a constant hydrogenation temperature of 150 °C for 30 minutes. As shown in Fig. 5b, the urchin-like $NiCo_2O_4$ structure liberated 0.14 and 0.37 wt% hydrogen from their adsorbed surface sites under the hydrogenation conditions of 6 and 10 bar, respectively. Meanwhile, $LiBH_4$ + 25% $NiCo_2O_4$, $LiBH_4$ + 50% $NiCo_2O_4$ and $LiBH_4$ + 75% $NiCo_2O_4$ systems desorbed 1.13, 1.67 and 2.48 wt% of H_2, respectively, for 6 bar pressure of hydrogenation. Moreover, under 10 bar hydrogenation condition, $LiBH_4$ + 25% $NiCo_2O_4$, $LiBH_4$ + 50% $NiCo_2O_4$ and $LiBH_4$ + 75% $NiCo_2O_4$ systems released 2.85, 3.78 and 3.91 wt% of H_2, respectively, from RT to 275 °C, as shown in Fig. 5c. From the above results, it can be inferred that the increased hydrogen sorption and desorption capacity of $LiBH_4/NiCo_2O_4$ systems are attributed to the increased hydrogenation pressure.

To determine the binding and kinetics nature of the hydrogenated (150 °C for 30 minutes under 10 bar) $LiBH_4/NiCo_2O_4$ systems, the activation and binding energies were calculated using Kissinger's[46–48] and van't Hoff[47,48] relations by analyzing the hydrogen desorption derivative thermogravimetric (DTG) curves. As shown in Fig. 5d, DTG curves exhibit the hydrogen desorption behaviour of $LiBH_4$ + 25% $NiCo_2O_4$, $LiBH_4$ + 50% $NiCo_2O_4$ and $LiBH_4$ + 75% $NiCo_2O_4$ systems at the H_2 desorption peak positions of 82.5, 67.9 and 66.4 °C, respectively. The corresponding activation energy (E_d) and binding energy (E_b) of the systems are, respectively, determined using the following equations:

$$\ln\left(T_p^2/\beta\right) = \frac{E_d}{RT_p}, \quad (1)$$

$$E_b = T_p \times K_B\left(\frac{\Delta S}{R}\right), \quad (2)$$

where T_p is the absolute temperature corresponding to the hydrogen desorption peak position, β is the heating rate, E_d is the activation energy, E_b is the 'binding energy of $1H_2$ molecule, K_B is the Boltzmann's constant, ΔS is the change in entropy

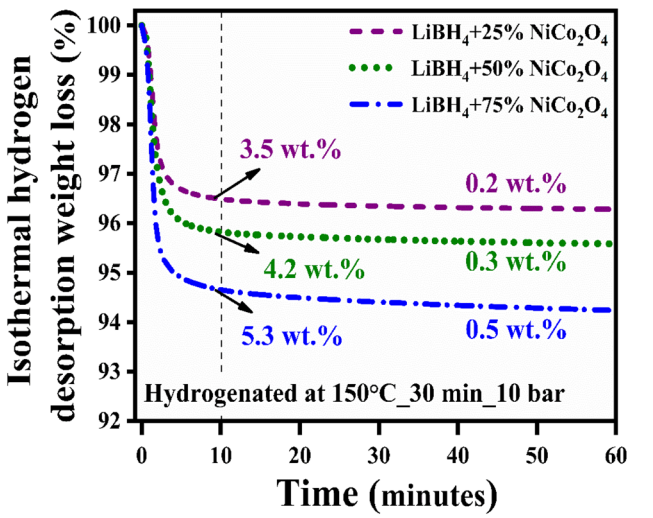

Fig. 6 Isothermal hydrogen desorption curves of $LiBH_4$ + 25% $NiCo_2O_4$, $LiBH_4$ + 50% $NiCo_2O_4$ and $LiBH_4$ + 75% $NiCo_2O_4$ systems.

Table 1 Hydrogen desorption characteristics of the systems under non-isothermal H_2 desorption conditions

Systems	Desorption peak temperature	Desorption capacity up to 275 °C	Binding energy (E_b)	Activation energy (E_d)
$LiBH_4$ + 25% $NiCo_2O_4$	82.5 °C	2.85 wt%	0.28 eV	17.99 kJ mol^{-1}
$LiBH_4$ + 50% $NiCo_2O_4$	67.9 °C	3.78 wt%	0.27 eV	17.03 kJ mol^{-1}
$LiBH_4$ + 75% $NiCo_2O_4$	66.4 °C	3.91 wt%	0.26 eV	16.92 kJ mol^{-1}

Table 2 Hydrogen storage properties of $LiBH_4$ catalyzed with spinel metal oxide structures

System	Synthesis method	Isothermal hydrogen desorption capacity	Ref.
$LiBH_4$ + $2LiNH_2$ + 0.05 wt% Co_3O_4	Ball milling at the argon-filled glove box	8.2 wt% (200 °C for 60 min)	53
$LiBH_4$ + $NiCo_2O_4$		3.8 wt% (250 °C for 50 min)	34
$LiBH_4$ + 9% mol $NiFe_2O_4$		2.4 wt% (300 °C for 20 min)	54
$LiBH_4$ + 20 wt% M-Fe_2O_3 + 30 wt% TiF_3		8.6 wt% (400 °C for 20 min)	55
$LiBH_4$ + 2ZnO/$ZnCo_2O_4$	Wet chemical impregnation at argon	3.1 wt% (300 °C for 60 min)	56
$LiBH_4$ + $NiMnO_3$		2.8 wt% (300 °C for 60 min)	57
$LiBH_4$ + 75% $NiCo_2O_4$ [a]	Wet chemical impregnation in the air	5.8 wt% (250 °C for 60 min)	This work
$LiBH_4$ + 50% $NiCo_2O_4$ [a]		4.5 wt% (250 °C for 60 min)	
$LiBH_4$ + 25% $NiCo_2O_4$ [a]		3.7 wt% (250 °C for 60 min)	

[a] Hydrogen desorption condition after hydrogenation.

(75.44 J mol^{-1} K^{-1}) and R is the 'gas constant'. The calculated activation and binding energies of the systems are presented in Table 1.

For an ideal hydrogen storage material, the binding energy of hydrogen should fall in the range of ~0.2–0.4 eV.[49–52] The recommended binding energy range for physisorption is ~0.01–

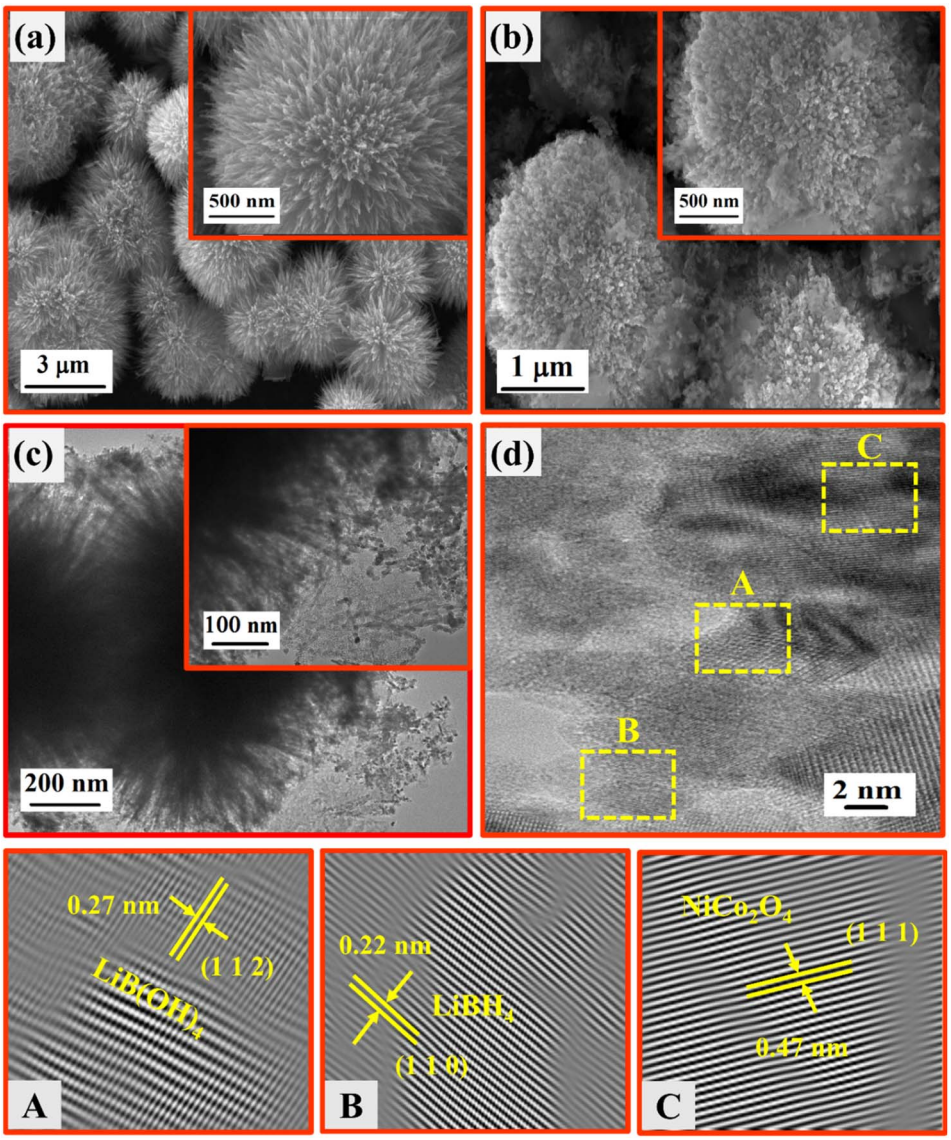

Fig. 7 SEM images of (a) $NiCo_2O_4$ and (b) $LiBH_4$ + 75% $NiCo_2O_4$; (c) TEM images of $LiBH_4$ + 75% $NiCo_2O_4$; (d) HRTEM images of $LiBH_4$ + 75% $NiCo_2O_4$.

0.1 eV and that for chemisorption is ~2–3 eV. As shown in Table 1, the activation and binding energies of the systems lie in the ranges 16.92–17.99 kJ mol^{-1} and 0.26–0.28 eV, respectively. As suggested by Silambarasan *et al.* and Ioannatos *et al.*, this desorption activation energy is close to the adsorption energy in the case of strong physisorption and/or weak chemisorption, which is in the range of 10–40 kJ mol^{-1}.[46,47] According to previous studies, it is clear that the H_2 is weakly chemisorbed on the $LiBH_4/NiCo_2O_4$ networks.

Hydrogenation and dehydrogenation cycle studies were investigated for the selected $LiBH_4$ + 75% $NiCo_2O_4$ system up to 5 times. Typically, hydrogenation experiments were carried out at 150 °C for 30 minutes under 10 bar pressure conditions for all hydrogenation cycles. Meanwhile, dehydrogenation cycle tests were conducted from RT to 275 °C under an argon atmosphere at a 15 °C min^{-1} heating rate. As shown in Fig. S1 (in ESI),† it was found to be ±0.25 wt% of variations in the H_2 release by the system (3.76 wt%). Additionally, H_2 sorption and desorption cycle tests confirm the stability of the systems, and further studies are required to evaluate their long-term performance.

Hydrogen desorption kinetics were studied under isothermal hydrogen desorption conditions at 250 °C for 60 minutes. Initially, the systems were hydrogenated at 150 °C for 30 minutes under 10 bar H_2 pressure. As shown in Fig. 6, the $LiBH_4$ + 75% $NiCo_2O_4$ system presented a higher desorption kinetics rate, and the capacity is 5.8 wt% in 60 minutes at 250 °C, while the $LiBH_4$ + 25% $NiCo_2O_4$ and $LiBH_4$ + 50% $NiCo_2O_4$ systems desorbed 3.7 and 4.5 wt% of hydrogen, respectively. Table 2 presents a comparison of the hydrogen desorption capacities of the $LiBH_4/NiCo_2O_4$ systems in this study with those in other studies.

As shown in Table 2, the other systems also hold significant desorption kinetics through the destabilization effect. However, they did not report the rehydrogenation and then hydrogen desorption. Among other systems, the surface oxidized $LiBH_4/NiCo_2O_4$ systems exhibit better hydrogen sorption kinetics.

3.3 Morphological and structural composition analyses

SEM and TEM analyses were employed to investigate the morphological and structural nature of the $NiCo_2O_4$ and $LiBH_4$ + 75% $NiCo_2O_4$ systems. As depicted in Fig. 7a, the SEM micrographs showed the urchin-like structure of $NiCo_2O_4$ with an average diameter of ~4 μm, which consisted of several ultrafine nanoneedles. This nanoneedles-assembled urchin-like structure is attributed to the surfactant used in the reaction, causing more active sites at the nucleation stage.[58] The SEM micrographs of the $LiBH_4$ + 75% $NiCo_2O_4$ system are shown in Fig. 7b, exhibiting a molten form of $LiBH_4$ with an urchin-like structure. TEM micrographs provide more insight

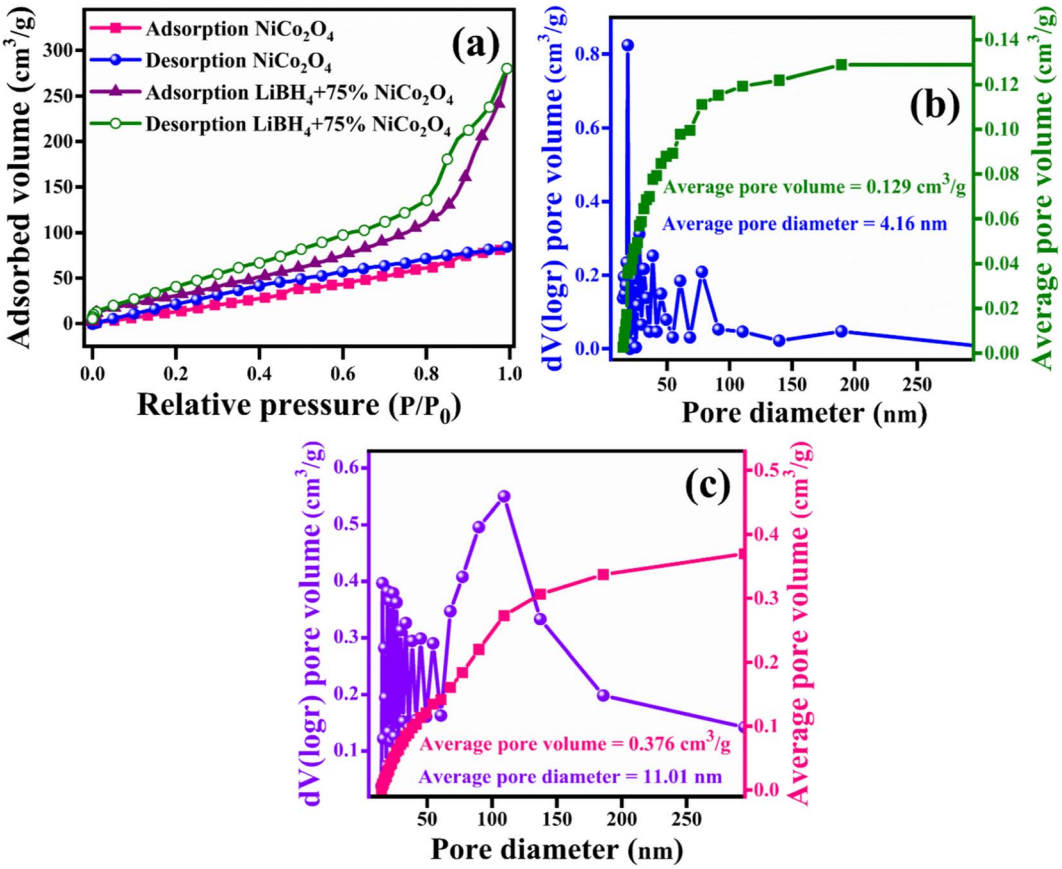

Fig. 8 (a) Nitrogen adsorption/desorption curves of $NiCo_2O_4$ and $LiBH_4$ + 75% $NiCo_2O_4$; BJH pore size distribution curves of (b) $NiCo_2O_4$ and (c) $LiBH_4$ + 75% $NiCo_2O_4$.

into the morphology and structure of the $LiBH_4$ + 75% $NiCo_2O_4$ system, as shown in Fig. 7(c) and (d). The average grain size is calculated as ~19 nm, as shown in Fig. S2 (in ESI).† The interplanar *d*-spacing determined from HRTEM images (Fig. 7d) of $LiBH_4$ + 75% $NiCo_2O_4$ system was 0.22, 0.27 and 0.47 nm,[59] which were assigned to the lattice planes of (1 1 0), (1 1 2) and (1 1 1) for the $LiBH_4$, $LiB[OH]_4$ and $NiCo_2O_4$ phases, respectively. Fig. S3 (in ESI)† shows the selected area electron diffraction (SAED) pattern of the $LiBH_4$ + 75% $NiCo_2O_4$ system, which showed that the polycrystalline nature and diffracted ring patterns agreed well with the XRD results.

3.4 Surface area analysis

For a better understanding of the H_2 storage mechanism, BET analysis was carried out to measure the specific surface area and porous properties of $NiCo_2O_4$ and $LiBH_4$ + 75% $NiCo_2O_4$ systems. As shown in Fig. 8a, the specific surface areas of $NiCo_2O_4$ and $LiBH_4$ + 75% $NiCo_2O_4$ systems were determined by N_2 adsorption/desorption isotherms. Both systems exhibit BET type IV isotherms. The BET surface areas for the $NiCo_2O_4$ and $LiBH_4$ + 75% $NiCo_2O_4$ systems were 124.05 and 136.62 $m^2\ g^{-1}$, respectively. As can be observed from the Barrett–Joyner–Halenda (BJH) pore size distribution curves, the $NiCo_2O_4$

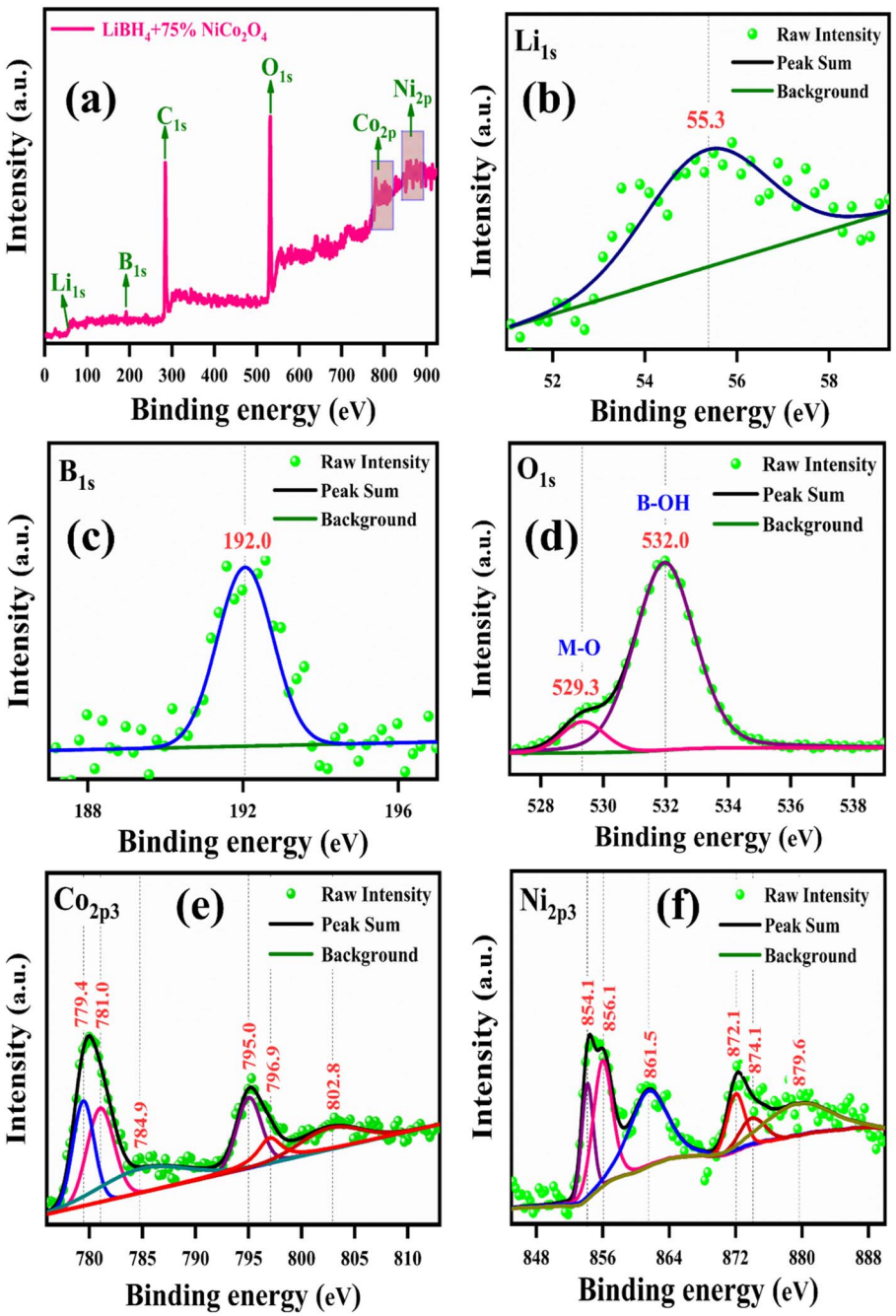

Fig. 9 XPS spectrum of $LiBH_4$ + 75% $NiCo_2O_4$: (a) survey spectrum, (b) Li 1s, (c) B 1s, (d) O 1s, (e) Co $2p_3$, and (f) Ni $2p_3$.

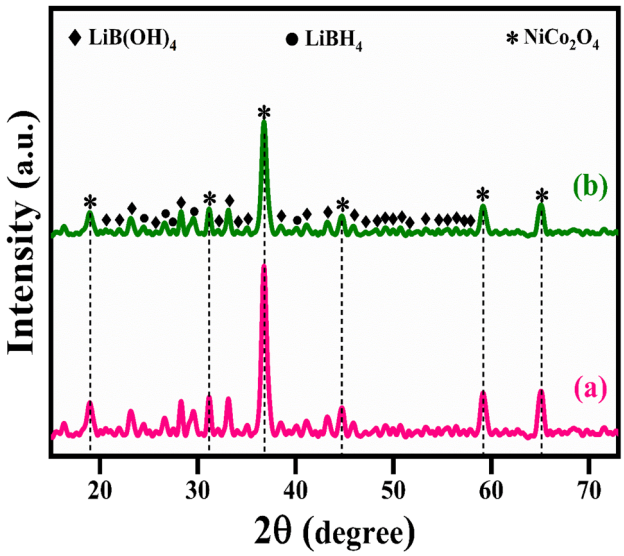

Fig. 10 XRD patterns of $LiBH_4$ + 75% $NiCo_2O_4$ (a) after hydrogenation (150 °C for 30 min under 10 bar) and (b) after dehydrogenation at 275 °C.

(Fig. 8b) and $LiBH_4$ + 75% $NiCo_2O_4$ (Fig. 8c) systems possess average pore volumes of 0.129 and 0.376 $cm^3\ g^{-1}$; they exhibit average pore diameters of 4.16 and 11.01 nm, respectively. After the addition of $NiCo_2O_4$, the surface area and porous nature of the systems are slightly increased, contributing favourable H_2 sorption and desorption to the $LiBH_4/NiCo_2O_4$ systems.

3.5 Elemental and compositional analysis

The binding energies and surface composition of the $LiBH_4$ + 75% $NiCo_2O_4$ system were analyzed by applying the X-ray photoelectron spectroscopy (XPS) technique. The survey spectrum and high-resolution spectra of Li 1s, B 1s, O 1s, Ni $2p_3$ and Co $2p_3$ are presented in Fig. 9. The survey spectrum illustrates the presence of Li, B, O, Co and Ni elements (Fig. 9a). The binding energy of Li 1s is observed at 55.3 eV (ref. 18 and 60) (Fig. 9b), while B 1s is located at 192.0 eV (ref. 18 and 61) (Fig. 9c). Additionally, the peaks of O 1s are observed at the binding energies of 529.3 and 532.0 eV,[59] which correspond to the typical metal–oxygen (M–O) and borohydroxide (B–OH) bonds, respectively (Fig. 9d). As shown in Fig. 9e, the high-resolution Co $2p_3$ spectrum is distributed into two Co species, that is the fitting peaks at 781.0 and 796.9 eV, which are attributed to the Co^{2+}, and the peaks located at 779.4 and 795.0 eV are assigned to the Co^{3+} components. Additionally, satellite peaks are observed at 784.9 and 802.8 eV.[62] Meanwhile, the Ni $2p_3$ spectrum is identified with Ni^{2+} and Ni^{3+} components having two satellite peaks. The deconvoluted peaks at 854.1 and 872.1 eV correspond to the Ni^{2+}, while the peaks at 856.1 and 874.1 eV are due to the Ni^{3+}. Moreover, the two satellite peaks

Table 3 Microstructural characteristics of the $LiBH_4$ + 75% $NiCo_2O_4$ system

Process	Average crystallite size (nm)	Average dislocation density ($\times10^{-3}$ nm^{-2})	Average micro strain ($\times10^{-3}$)
Hydrogenated at 150 °C for 30 minutes under 10 bar	58	2.95	5.11
Dehydrogenated at 275 °C	55	3.15	5.49

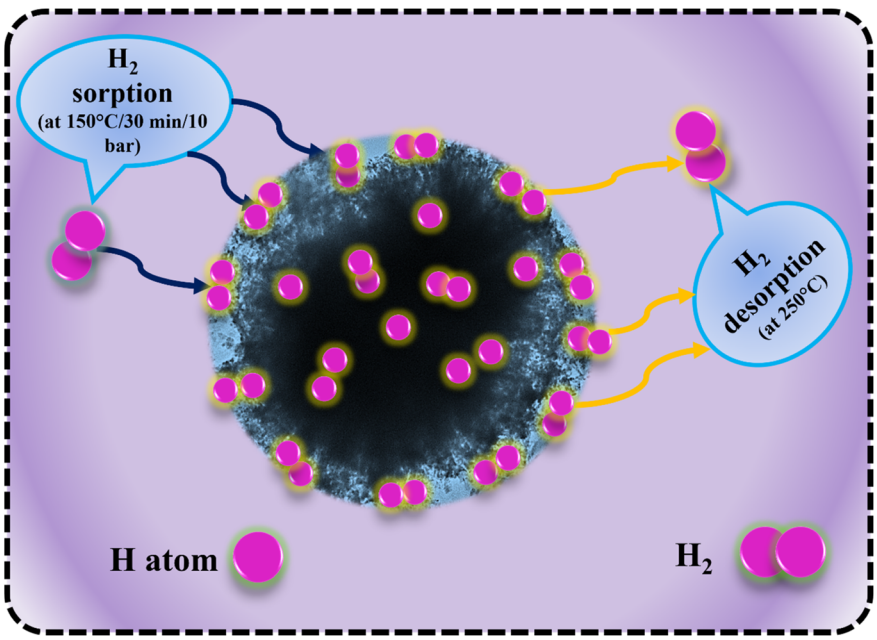

Fig. 11 Hydrogen sorption and desorption mechanisms of $LiBH_4/NiCo_2O_4$ systems.

are observed at binding energies of 861.5 and 879.6 eV (ref. 62) for Ni $2p_3$, as shown in Fig. 9f.

3.6 Structural analysis after hydrogenation, dehydrogenation and rehydrogenation

The microstructural changes in the $LiBH_4$ + 75% $NiCo_2O_4$ system were characterized by XRD analysis after hydrogenation and dehydrogenation processes. Fig. 10(a) and (b) show the XRD pattern of the $LiBH_4$ + 75% $NiCo_2O_4$ system after hydrogenation and dehydrogenation. Slight changes in peak intensities suggest the lattice rearrangement and defect refinement induced by the presence of hydrogen molecules.[57,63] No structural changes were observed in the $LiBH_4$ + 75% $NiCo_2O_4$ system after hydrogenation and dehydrogenation.[64] The average crystallite size (D), microstrain (ε) and dislocation density (δ)[65–69] are presented in Table 3. From the structural analysis, it can be inferred that the hydrogen charging and discharging conditions did not alter the phase structures of the systems. Further theoretical and experimental investigations on these systems would lead to a better understanding of catalytic and synergistic mechanisms.

Fig. 11 illustrates the schematic diagram of hydrogen sorption and desorption mechanisms for $LiBH_4/NiCo_2O_4$ systems. During hydrogenation, hydrogen molecules diffused through the surface pores, reaching the interfaces of $LiBH_4/NiCo_2O_4$ systems. It is expected that hydrogen can be absorbed in molecular and dissociated forms. In the following dehydrogenation process, the absorbed H_2 molecules/hydrogen ions from the surfaces and interfaces of $LiBH_4/NiCo_2O_4$ systems were desorbed at a dehydrogenation temperature of 275 °C. This suggests that the increased concentration of $NiCo_2O_4$ in the system impacts the active sites of $LiBH_4/NiCo_2O_4$ systems and causes improved storage capacity.

4 Conclusion

The mesoporous $NiCo_2O_4$ was synthesized using the hydrothermal method, and a simple ultrasonication-assisted wet-impregnation method was used for the preparation of $LiBH_4/NiCo_2O_4$ hydrogen storage systems. The physico-chemical properties were studied using XRD, FTIR, XPS, SEM, TEM, BET and TGA analyses. Furthermore, hydrogenation experiments were performed for the $LiBH_4$ + $NiCo_2O_4$ systems at a hydrogenation temperature of 150 °C for 30 min under different pressures. From the non-isothermal dehydrogenation results, $LiBH_4$ + 25% $NiCo_2O_4$, $LiBH_4$ + 50% $NiCo_2O_4$ and $LiBH_4$ + 75% $NiCo_2O_4$ systems exhibited the hydrogen release of 2.85, 3.78 and 3.91 wt%, respectively. Isothermal dehydrogenation of the hydrogenated $LiBH_4$ + 75% $NiCo_2O_4$ system at 250 °C released ~5.8 wt% of hydrogen in 60 minutes. The addition of $NiCo_2O_4$ significantly enhanced the dehydrogenation kinetics of the surface oxidized $LiBH_4$ system. Moreover, the estimated hydrogen binding energy of the $LiBH_4/NiCo_2O_4$ systems lies in the range of 0.26–0.28 eV. Therefore, it can be inferred that the interaction between H_2 molecules and $LiBH_4/NiCo_2O_4$ systems is weak chemisorption or strong physisorption. The remarkable hydrogen storage performance was shown by the $LiBH_4$ + 75% $NiCo_2O_4$ system possibly due to the larger surface area, porosity and favourable electronic environment of $NiCo_2O_4$. Moreover, these results provide new opportunities to consider $LiBH_4/NiCo_2O_4$ systems as an economical and prospective material for hydrogen charging/discharging applications.

Data availability

The data supporting this article are included in ESI.†

Author contributions

Ajaijawahar Kaliyaperumal: conceptualization, methodology, data curation, formal analysis, writing – original draft, writing – review & editing. Gokuladeepan Periyasamy: formal analysis, validation, writing – review & editing. Iyakutti Kombiah: formal analysis, validation, investigation, writing – review & editing. Karthigeyan Annamalai: conceptualization, resources, investigation, supervision, writing – original draft, writing – review & editing.

Conflicts of interest

There are no conflicts of interest to declare.

Acknowledgements

The authors acknowledge the SCIF, SRMIST for providing the instrumentation facilities. The authors would like to acknowledge the PNCF and NRC, SRM IST for providing the characterization facilities.

References

1 J. Wang and A. Waseem, *Geosci. Front.*, 2024, **15**, 101757.
2 X. Liu, S. Bo, P. Lynn, H. Ali, L. Hongyou, Y. Cong and F. Guanyun, *Wiley Interdiscip. Rev.: Energy Environ.*, 2019, **8**, e342.
3 K. O. D. Yoro and O. Michael, in *Advances in Carbon Capture*, Elsevier, 2020, pp. 3–28, DOI: **10.1016/B978-0-12-819657-1.00001-3**.
4 B. C. N. Tashie-Lewis and S. G. Nnabuife, *Chem. Eng. J. Adv.*, 2021, **8**, 100172.
5 M. G. Rasul, M. A. Hazrat, M. A. Sattar, M. I. Jahirul and M. J. Shearer, *Energy Convers. Manage.*, 2022, **272**, 116326.
6 O. Faye, S. Jerzy and E. Ubong, *Int. J. Hydrogen Energy*, 2022, **47**, 13771–13802.
7 R. Rameshbabu, P. Johnny Koh Siaw, K. Ajaijawahar, V. Victor, J. Sapana, P. Nalandhiran and K. Tiong Sieh, *J. Alloys Compd.*, 2024, **997**, 174830.
8 S. R. Bosu, *Int. J. Hydrogen Energy*, 2024, **52**, 352–370.
9 K. Nivedhitha, T. Beena, N. R. Banapurmath, M. A. Umarfarooq, R. Venkatesh, M. E. M. Soudagar and A. Ümit, *Int. J. Hydrogen Energy*, 2024, **61**, 1259–1273.
10 C. Tarhan and Ç. Mehmet Ali, *J. Energy Storage*, 2021, **40**, 102676.

11 H.-J. Lin, L. Hai-Wen, S. Huaiyu, L. Yanshan and A. Kohta, *Mater. Today Energy*, 2020, **17**, 100463.
12 M. S. Salman, L. Qiwen, L. Xiaoxuan, P. Chulaluck, R. Nigel, C. Mehdi, W. Ting, S. Prabal, L. Wei and G. Aiden, *Journal of Alloys and Compounds*, 2022, **920**, 165936.
13 J. Liu, M. Yong, Y. Jinggang, S. Lei, G. Dongliang and X. Peng, *Front. Chem.*, 2022, 982, DOI: **10.3389/fchem.2022.945208**.
14 X. Zhang, Z. Wenxuan, Z. Lingchao, H. Zhenguo, H. Jianjiang, G. Mingxia, P. Hongge and L. Yongfeng, *Chem. Eng. J.*, 2022, **428**, 132566.
15 Y. Huang, Z. Yun, L. Jianding, B. Xiaozhi, G. Junpo, S. Jingjun, G. Yan, Z. Qi, L. Jing and L. Wen, *J. Mater. Sci. Technol.*, 2023, **153**, 181–204.
16 C. Li, P. Peng, D. W. Zhou and L. Wan, *Int. J. Hydrogen Energy*, 2011, **36**, 14512–14526.
17 J. Goudon, F. Bernard, J. Renouard and P. Yvart, *Int. J. Hydrogen Energy*, 2010, **35**, 11071–11076.
18 L. Vellingiri, A. Karthigeyan, K. Ramamurthi and K. Iyakutti, *RSC Adv.*, 2019, **9**, 31483–31496.
19 A. Kaliyaperumal, V. Lathapriya, P. Gokuladeepan and A. Karthigeyan, *J. Mater. Sci.: Mater. Electron.*, 2022, **33**, 9144–9154.
20 Y. Fan, C. Dandan, Y. Zhenluo, C. Qiang, F. Guangxin, Z. Dan and L. Baozhong, *Front. Chem.*, 2020, **8**, 45.
21 T. C. Lee, S. C. John, W. Lin and D. Eric, *ACS Appl. Energy Mater.*, 2021, **4**, 9742–9750.
22 A. M. Beaird, A. D. Thomas and M. A. Matthews, *Ind. Eng. Chem. Res.*, 2010, **49**, 9596–9599.
23 M. Murtomaa, E. Laine, J. Salonen and O. Kuusinen, *Powder Handling Process.*, 1999, **11**, 87–90.
24 C. Haertling, R. J. Hanrahan Jr and R. Smith, *J. Nucl. Mater.*, 2006, **349**, 195–233.
25 P. Mauron, B. Florian, F. Oliver, R. Arndt, B. Michael, C. N. Zwicky and Z. Andreas, *J. Phys. Chem. B*, 2008, **112**, 906–910.
26 J. J. Vajo, L. S. Sky and M. Florian, *J. Phys. Chem. B*, 2005, **109**, 3719–3722.
27 H. Yuan, Z. Xugang, L. Zhinian, Y. Jianhua, G. Xiumei, W. Shumao, L. Xiaopeng and J. Lijun, *Int. J. Hydrogen Energy*, 2012, **37**, 3292–3297.
28 M. Cabo, G. Sebastiano, P. Eva, M. Chiara, G. Alessandro, M. Amedeo, R. Emma, S. Santiago and B. Maria Dolors, *Int. J. Hydrogen Energy*, 2011, **36**, 5400–5410.
29 X. Yu, D. M. Grant and G. S. Walker, *J. Phys. Chem. C*, 2009, **113**, 17945–17949.
30 H. Zhang, C. Zhong, S. Li-Xian, S. Yu-Jia, X. Fen, L. Hui, Z. Jian, H. Zi-Qiang, J. Xia and L. Zhi-Bao, *J. Therm. Anal. Calorim.*, 2013, **112**, 1407–1414.
31 Y. Zhang, L. Yongfeng, P. Yuepeng, G. Mingxia and P. Hongge, *J. Mater. Chem. A*, 2014, **2**, 11155–11161.
32 Y. Zhang, Z. Wan-Sheng, F. Mei-Qiang, L. Shu-Sheng, C. Hai-Liang, Z. Yan-Hua, G. Xiu-Ying and S. Li-Xian, *J. Phys. Chem. C*, 2008, **112**, 4005–4010.
33 M. Au, S. William, J. Arthur and Z. Christine, *J. Alloys Compd.*, 2008, **462**, 303–309.
34 L. Zang, Z. Qiuyu, L. Li, H. Yike, C. Xiaoya, J. Lifang, Y. Huatang and W. Yijing, *Chem.–Asian J.*, 2018, **13**, 99–105.
35 Y. Zhang, L. Yongfeng, L. Tao, G. Mingxia and P. Hongge, *Int. J. Hydrogen Energy*, 2013, **38**, 13318–13327.
36 J. Shao, X. Xuezhang, C. Lixin, F. Xiulin, L. Shouquan, G. Hongwei and W. Qidong, *J. Mater. Chem. A*, 2012, **22**, 20764–20772.
37 G. Xia, Y. H. Guo, Z. Wu and X. B. Yu, *J. Alloys Compd.*, 2009, **479**, 545–548.
38 F. K. Butt, T. Muhammad, C. Chuanbao, I. Faryal, R. Ahmed, W. S. Khan, A. Zulfiqar, M. Nasir, M. Tanveer and M. Asif, *ACS Appl. Mater. Interfaces*, 2014, **6**, 13635–13641.
39 F. K. Butt, C. Chuanbao, I. Faryal, T. Muhammad, H. Rafaqat, R. Ahmed and W. S. Khan, *Int. J. Hydrogen Energy*, 2015, **40**, 9359–9364.
40 A. Kaliyaperumal, P. Gokuladeepan and A. Karthigeyan, *Int. J. Hydrogen Energy*, 2023, **50**, 812–826.
41 J. K. Kang, K. Se Yun, H. Young Soo, R. P. Muller and W. A. Goddard III, *Appl. Phys. Lett.*, 2005, **87**, 111904.
42 S. Kato, B. Michael, B. Andreas, V. Zakaznova-Herzog, R. Arndt, O. Shin-ichi and Z. Andreas, *Phys. Chem. Chem. Phys.*, 2010, **12**, 10950–10955.
43 J. Carrillo-Bucio, T.-G. Juan, L. Rogelio and K. Suárez-Alcántara, *Inorganics*, 2017, **5**, 82.
44 V. Venkatachalam, A. A., A. Alghamdi and R. Jayavel, *Ionics*, 2017, **23**, 977–984.
45 T. Wang and K. F. Aguey-Zinsou, *Energy Technol.*, 2019, **7**, 1801159.
46 G. E. Ioannatos and E. V. Xenophon, *Int. J. Hydrogen Energy*, 2010, **35**, 622–628.
47 D. Silambarasan, V. J. Surya, V. Vasu and K. Iyakutti, *Int. J. Hydrogen Energy*, 2013, **38**, 4011–4016.
48 L. Vellingiri, A. Karthigeyan, K. Ramamurthi and K. Iyakutti, *Int. J. Hydrogen Energy*, 2018, **43**, 10396–10409.
49 E. Klontzas, T. Emmanuel and G. E. Froudakis, *J. Phys. Chem. Lett.*, 2011, **2**, 1824–1830.
50 R. C. Lochan and H.-G. Martin, *Phys. Chem. Chem. Phys.*, 2006, **8**, 1357–1370.
51 R. Rameshbabu, K. Siaw Paw, K. Ajaijawahar, J. Sapana, A. John, Y. Chong Tak, T. Sieh Kiong and Y. Talal, *Int. J. Hydrogen Energy*, 2024, **61**, 743–753.
52 G. Periyasamy, K. Ajaijawahar, R. Rameshbabu and A. Karthigeyan, *J. Mater. Sci.: Mater. Electron.*, 2024, **35**, 1–11.
53 Y. Zhang, L. Yongfeng, P. Yuepeng, G. Mingxia and P. Hongge, *J. Mater. Chem. A*, 2014, **2**, 11155–11161.
54 J. Zhang, P. Li, Q. Wan, F. Zhai, A. A. Volinsky and X. Qu, *RSC Adv.*, 2015, **5**, 81212–81219.
55 H. Zhang, Z. Cao, L.-X. Sun, Y.-J. Sun, F. Xu, H. Liu, J. Zhang, Z.-Q. Huang, X. Jiang and Z.-B. Li, *J. Therm. Anal. Calorim.*, 2013, **112**, 1407–1414.
56 X. Xu, Z. Lei, Z. Yaran, Z. Yan, W. Yijing and J. Lifang, *J. Power Sources*, 2017, **359**, 134–141.
57 X. Xu, Z. Lei, Z. Yaran, L. Yongchang, W. Yijing and J. Lifang, *Int. J. Hydrogen Energy*, 2017, **42**, 25824–25830.
58 J. Wang, Z. Yangyang, Y. Junhua, W. Hongmei, H. Jinghua, M. Juyi, Z. Shuoqing and H. Shahid, *RSC Adv.*, 2016, **6**, 70077–70084.

59 Y. Zhang, Z. Yihe, Z. Deyang and S. Li, *Dalton Trans.*, 2017, **46**, 9457–9465.
60 M. Shek, J. Hrbek, T. K. Sham and G.-Q. Xu, *Surf. Sci.*, 1990, **234**, 324–334.
61 X. Lü, W. Jianjun, L. Tianquan, W. Dongyun, H. Fuqiang, X. Xiaoming and J. Mianheng, *J. Mater. Chem.*, 2011, **21**, 10685–10689.
62 J. Zhang, M. Qianwen, D. Yaping, G. Kai, Y. Xinxin and Z. Jingtai, *ACS Appl. Mater. Interfaces*, 2017, **9**, 29771–29781.
63 K. Xian, N. Bo, L. Zigen, G. Mingxia, L. Zhenglong, S. Congxiao, L. Yongfeng, G. Zhengxiao and P. Hongge, *Chem. Eng. J.*, 2021, **407**, 127156.
64 J. Shao, X. Xuezhang, F. Xiulin, Z. Liuting, L. Shouquan, G. Hongwei, W. Qidong and C. Lixin, *J. Phys. Chem. C*, 2014, **118**, 11252–11260.
65 S. Mustapha, M. M. Ndamitso, A. S. Abdulkareem, J. O. Tijani, D. T. Shuaib, A. K. Mohammed and A. Sumaila, *Adv. Nat. Sci.: Nanosci. Nanotechnol.*, 2019, **10**, 045013.
66 K. Maniammal, G. Madhu and V. Biju, *Phys. E*, 2017, **85**, 214–222.
67 P. Bindu and T. Sabu, *J. Theor. Appl. Phys.*, 2014, **8**, 123–134.
68 S. K. Sen, B. Utpal Chandra, M. S. Manir, M. Pritish, D. Supria, P. Mollika, M. A. M. Chowdhury and M. A. Hakim, *Adv. Nat. Sci.: Nanosci. Nanotechnol.*, 2020, **11**, 025004.
69 E. Karvannan, V. V., T. S. Nivin, J. Archana, M. Navaneethan and A. Karthigeyan, *Mater. Chem. Phys.*, 2024, **312**, 128506.